LAWRENCE
LIVERMORE
NATIONAL
LABORATORY

UCRL-CONF-230236

Explosively driven facture and fragmentation of metal cylinders and rings

D.M. Goto, R. C. Becker, T. J. Orzechowski, H. K. Springer, A. J. Sunwoo, C. K. Syn

April 24, 2007

Hypervelocity Impact Symposium-2007
Williamsburg, VA, United States
September 23, 2007 through September 27, 2007

Disclaimer

UCRL-CONF-230236

Investigation of the fracture and fragmentation of explosively driven rings and cylinders

D. M. Goto, R. C. Becker, T. J. Orzechowski, H. K. Springer, A. J. Sunwoo, C. K. Syn

Lawrence Livermore National Laboratory
Livermore, CA 94550

Abstract

Cylinders and rings fabricated from AerMet® 100 alloy and AISI 1018 steel have been explosively driven to fragmentation in order to determine the fracture strains for these materials under plane strain and uniaxial stress conditions. The phenomena associated with the dynamic expansion and subsequent break up of the cylinders are monitored with high-speed diagnostics. In addition, complementary experiments are performed in which fragments from the explosively driven cylinder are recovered and analyzed to determine the statistical distribution associated with the fragmentation process as well as to determine failure mechanisms. The data are used to determine relevant coefficients for the Johnson-Cook (Hancock-McKenzie) fracture model. Metallurgical analysis of the fragments provides information on damage and failure mechanisms.

1. Introduction

Explosively driven fragmentation of ductile metals is a highly complex phenomenon in which the fragmenting material is plastically deformed by the passage of an intense shock (~10's of GPa) followed by tensile deformation and expansion to failure. The process is much more involved than simple quasistatic tensile failure and fracture, which has been studied for more than a century. This dynamic subject has been of interest to researchers for decades, with much of the seminal work, which focused on mechanical

performance, fragment-size distribution, fracture strain and failure mechanisms starting during the Second World War. It is of particular interest in the design of munitions and armaments.

G. W. Gurney estimated the terminal velocities of (metal) case materials for spheres, cylinders and infinite planes driven by enclosed high explosives [1]. These terminal velocities are functions of the metal case mass to high-explosive mass ratio and the energy of the high explosive available to drive the material. In spite of shortcomings due to lack of material strength and early release of gas pressure due to fragmentation of the case, his formulae give very good estimates of these terminal velocities. G. I. Taylor studied tubular bombs and specifically tubular bombs driven from one end [2]. He gave analytic estimates of the opening angle of these cylindrical bombs as a function of radial expansion of the metal wall (which can be estimated from the Gurney velocity) and the detonation velocity of the explosive, which is determined from the equation of state of the high explosive. Again, his analytic approximations are in reasonable agreement with more precise numerical simulations and experiment.

N. F. Mott developed a model to calculate the size and the mass of the fragments in an expanding ring or cylinder [3]. His model to determine fragment size postulates a failure strain and a distribution in failure strain, and then stops the fracture of material that is subsumed by a stress release wave that propagates through the fractured material.

During this same period, G. I. Taylor developed a model of fracture strain for tubular bombs based on the tensile strength of the material, the internal pressure in the bomb, and thickness of the steel tube encasing the explosive [4]. In this model the fractures occur on the outside of the case and propagate inward as the stresses in the material go from compressive to tensile.

These early works laid the foundation for a field of study that continues to this day. The literature on this topic is extensive, and we cannot adequately report all of the work that has been done in this field over the past half century[5-10]. In addition to driving the material with high explosives, gas guns [11,12] and magnetic drive [13] have also been employed to study the phenomenon of high-rate fracture and fragmentation. However, these latter experiments (gas gun and magnetic drive) do not subject the material to the high pressures that the explosive does.

In the work presented here, we investigate the fracture and fragmentation of AerMet® 100 alloy [14] and AISI 1018 steel. The material is driven by an explosive for the express purpose of determining the strain at failure at a single strain rate for two different load paths. The cylindrical geometry of the experiment allows for relatively easy analysis, both computationally and analytically. In addition to metal cylinders, we conduct experiments using metal rings to change the stress history of the sample. Metallurgical analysis of the fragments reveals failure mechanisms that can support the physics based failure models.

2. Cylinder design, modeling and simulation

The experiments discussed in this paper are designed to investigate the failure and fragmentation of ductile-metals that are explosively driven and subjected to strain rates between 10^4 s^{-1} and $10^5 s^{-1}$, and load paths characterized by initially plane-strain and uniaxial-stress conditions. We are interested in determining the fracture strain of the material under these load paths and determining the dominant failure mechanisms. Load path (stress triaxiality), as well as strain-rate, are integral to some of the failure models currently in use. A thin walled cylinder subjected to purely radial expansion has a stress triaxiality of 0.577, corresponding to a plane-strain condition. This can be compared with a spherical surface that experiences a triaxiality of 0.667 when loaded uniformly from the inside (biaxial strain), or a ring that experiences a triaxiality of 0.33 when expanding uniformly in the radial direction (uniaxial strain).

An axisymmetric cylindrical geometry is used in the current experiments. The cylinder has an outer diameter of 5.08-cm. The wall thickness of the metal cylinder is 0.3 cm. Two different lengths of cylinder are used in order to affect the load path. A nominal cylinder length of 20.32 cm is used to achieve a plane strain load path, whereas a 0.3 cm long cylinder (ring) is used to achieve a uniaxial stress load path. In this latter case, a number of individual rings are stacked onto the high explosive charge to improve the statistics of the fragment recovery experiments. The cylinders are fabricated from either AerMet® 100 alloy or AISI 1018 steel. The cylinder and ring geometries are shown schematically in Figures 1a and 1b. The cylinder or a stacked set of twenty five rings is filled with a high explosive, LX-17. In the case of the ring array, copper sleeves are placed before and after the array to achieve an effective length of 20.32 cm, and to confine the high explosive (HE) as the detonation wave passes down the cylinder. The high explosive is bonded into the

cylinder (or ring assembly) with a silastic epoxy nominally 50 μm thick. A frustum shaped booster comprising a conventional high explosive, LX-10, initiates the LX-17 main charge at one end. The purpose of this booster is to provide a near-planar detonation to the main charge. The case-mass to charge-mass ratio (M/C) for this configuration is 1.18. The Gurney velocity for a finite length cylinder is given by [15]:

$$V_G = \sqrt{\frac{2E_o}{\left[\frac{M}{C}+\frac{1}{2}\right]\left[1+\frac{R_c}{L_c}\right]}}, \qquad (1)$$

where V_G is the final velocity of the metal case, E_o is the detonation energy of the explosive, R_c is the radius of the cylinder and L_c is its length. Using the listed value of 3628 J/g for the detonation energy of LX-17 [16], the Gurney velocity of this metal case, for a finite length cylinder is 1.9 mm/μs. At this radial velocity, the strain rate is about $7x10^4$/s. Because the cylinder is detonated at one end, it expands in a cone-shaped geometry with an opening angle of the cone given by the Taylor angle and is approximately 14°. This value is somewhat larger than the simulated and measured value of 11°; the overestimate of opening angle in this simple model is probably due to the absence of material strength.

The exploding cylinder is modeled with the two-dimensional hydrodynamics code CALE [17]. Because this code and the associated model are 2-D, it cannot accurately simulate the fracturing of the cylinder. However, the results from the calculation help in understanding the dynamics associated with the shock passing through the cylinder wall and the complex stress and strain histories associated with this transient event. A Gruneisen equation of state and a Steinberg-Guinan [18] constitutive model describe the physical and material properties of the metal cylinder. Material failure, being an intrinsically 3-D phenomenon, was not modeled in the design of these experiments. However, the data measured from the experiments is used to calibrate a statistics-compensated Johnson-Cook fracture model [19], which is currently implemented in a variety of hydrodynamic computer codes.

CALE simulations allow us to evaluate the time dependent pressure, densities and material properties as the detonation wave traverses the cylinder. The simulations provide information on the uniformity of the deformation along the axis of the cylinder. This is of particular importance in the fragment recovery experiments. Because, we do not know which part of the cylinder any individual fragment came from, it is

important to know how uniform the load path is along the cylinder. The high explosive shock imparts a significant transient deformation to the metal as the shock sweeps along the cylinder. The simulations indicate that the peak density in the cylinder wall in the vicinity of the shock is about 8.6 g/cm^3—about 10% higher than the nominal alloy density. In the simulation, the radial velocity asymptotes to a value of about 1.65 cm/μs (except for the location near the front of the cylinder which asymptotes to a slightly lower value due to the reduced drive pressure near the open end of the cylinder). CALE simulations without material strength show the case velocity asymptote to a value of 1.75 cm/μs. The simulation shows the detonation front to be fairly planar with a grazing angle at the interior of the cylinder wall. Figure 2 shows the pressure contours in the cylinder at t=15 μs. Peak pressure in the shock front is about 26 GPa; the CJ pressure for LX-17 is 28 GPa. Careful examination of the shock wave in the metal cylinder at the axial position of the detonation wave shows the shock angle to be about 52° to the wall normal. This corresponds roughly to the angle whose tangent equals the ratio of the sound speed in AerMet®-100 alloy to the LX-17 detonation velocity: $\tan^{-1}$(5.78 mm/μs:7.6 mm/μs). The shock in the cylinder wall is illustrated in the inset in Figure 2. The pressure in the metal cylinder behind the shock front oscillates as the shock wave reflects off the outer and inner surfaces of the cylinder. Finally, at late times, after the driving pressure is near zero, the pressure in the wall asymptotes to about -700 MPa, which corresponds to 700 MPa in tension.

CALE also provides information on the stress state and equivalent plastic strain (eps) and strain rate at various times and locations. The load path, which is illustrated by the eps versus stress triaxiality (defined as the ratio of pressure to von Mises stress), is shown in Figure 3 for three positions along the cylinder. The location at which the load path is calculated is determined by specifying a tracer particle in the cylinder wall. CALE follows this tracer particle and computes the desired parameter, in this case, stress triaxiality, at that location. As can be seen from the simulation, each section of the cylinder along the axis experiences the same stress history, only at different times depending on when the detonation wave reaches that location along the cylinder. Initially, the material is highly compressed by the HE shock wave. (In the convention here, negative triaxiality is compression and positive triaxiality is tension). After the shock passes, the material goes into tension. It is in this tensile state that the material fails and breaks.

We have also used CALE to simulate the thinning of the metal wall due to cylinder expansion as a function of time via tracer particles on the inner and outer surface of the metal cylinder in the simulation. This calculated through-thickness strain resulting from the wall thinning is shown in Figure 4 along with the eps as a function of time. There is a near constant offset between the two curves and this is attributed to the plastic strain accumulated during the passage of the initial shock at the beginning of the event as the material is plastically deformed (compressed and decompressed). This calculated difference between eps and thickness strain is crucial in determining the eps at fracture for the cylinder--in measuring the strain at failure we actually measure the thickness of the fragment and relate it to the eps through the simulation results. We should point out here that our thickness measurement of the fragments gives a *net* strain at fracture, which is related but not identical to the equivalent plastic strain at fracture.

3. Cylinder materials

The cylinder cases used in the experiments described here are fabricated from either AerMet® 100 alloy or AISI 1018 steel. Two very different materials are studied, where the former is a high strength, high toughness alloy, and the latter is a low strength and ductile steel.

The martensitic microstructure in AerMet® 100 alloy, in concert with the second phase precipitates, provides its high strength and high toughness. After a multi-step heat treatment (HT), the material's hardness increased from a Rockwell C value of 40 to 55. Selected material properties are presented in Table 1. The microstructure of the HT alloy, shown in Figure 5a, comprises a fine lenticular structure of martensite. Submicron size metallic carbide particles, precipitated during the heat treatment, decorate the martensite boundaries [20]. In addition, micron-sized inclusions (Ø~1.5 μm ± 0.8 μm) comprising rare earth elements, namely Ce and La, are observed (Figure 6a-insert). A detailed SEM analysis of an AerMet® 100 alloy sample indicates an inclusion density of about $3.5 \times 10^5/cm^3$. In ductile microvoid fracture, these spheroidal inclusions can be effective nucleation sites for void formation.

A medium carbon steel, AISI 1018, was purchased as a hot rolled and annealed round 15.24 cm (6") bar stock. Slow cooling from a hot-rolling process produces a low strength steel with modest ductility. An average Vickers hardness number for 1018 steel is $135 kg/mm^2$. The microstructure of the steel contains dual

phases of ferrite grains and pearlite colonies. Pearlite is a lamella of ferrite and cementite (Fe_3C). Also visible in the microstructure is MnS inclusion particles and stringers. In contrast to the metallic carbide particles in the AerMet® 100 alloy, MnS inclusions do not contribute to the strength or ductility of the steel. Instead, they tend to promote premature failure. Moreover, the ferrite grains are significantly larger with a random distribution of pearlite, which may also contribute to the lower strength. Figure 5b displays the microstructure of the AISI 1018 steel consisting of ferrite, pearlite, and MnS inclusions. Elastic and quasistatic tensile properties of the AISI 1018 steel are also summarized in Table 1.

4. Experiment design

The experiments discussed here were conducted in two different series. In one series, real-time information was collected using high-speed diagnostics that include high-speed framing cameras (1frame/μs), flash radiography and velocimetry of the outer surface of the metal cylinder. A second series of experiments was designed to recover as many of the cylinder fragments as possible. For these experiments, the cylinder or ring array is surrounded by an octagonal foam box immersed in a water tank. When fielding the soft-recovery experiments, no high-speed diagnostics were employed.

High-speed optical imaging used Cordin 121E1 and 140E1 framing cameras. Both of these cameras can provide images at a rate of 1-frame per μs. The Cordin 121E1 camera provides 26 images on 70-mm film while the 140E1 can provide 60 images using 35-mm film. The cylinder is illuminated using Gigalumen® flash lamps. The radiograph uses x-rays generated by a nominal 1.5-MeV electron beam and provides a dose of approximately 0.25 rad at 1-m. The spot size is about 1-mm diameter. The object is located 2.5 m from the Tungsten target and the film pack is placed 0.5 m beyond the object providing an image with a magnification of 1.2. The expanding cylinder is imaged orthogonally to the axis of symmetry, thus the x-rays pass through two walls of the cylinder and produce a double-pass image. Doppler shifted velocimetry monitors the wall motion at four locations along the cylinder.

Fragment-recovery experiments are performed separately from the real-time diagnostics experiments because the recovery apparatus precludes direct observation of the event. A schematic of the recovery system is shown in Figure 6. The cylinder or ring array is located at the center of the capture chamber. Surrounding

the cylinder is an octagonal shaped box constructed of 10.5 cm thick foam that has a density of 0.32 g/cm^3. This octagonal chamber is 95 cm across (inside dimension) and 61 cm high. This allows for approximately 45 cm of air between the cylinder and the foam wall. A 25-cm thick foam lid is placed on top of the foam box. The foam box is contained within a plastic tank that has a 2.74-m diameter. The region between the foam box and the plastic tank is filled with water to a depth of 60 cm so that the fragments are completely stopped before reaching the plastic tank. The capture mechanism is designed so that the fragments are retarded with a pressure well below the ultimate tensile strength of the steel.* After the test, most of the fragments are collected from within the plastic tank (*i.e*. the water). A smaller fraction of the fragments are stopped in the foam. In spite of the effort to capture all the metal fragments, about 10 to 30% of a cylinder is not recovered.

After the fragments are retrieved, they are cleaned, weighed, measured and a subset is characterized metallographically. Most of the fragments are weighed individually. A large number of fragments (making up a small fraction of the total mass of the recovered fragments) weigh less than 0.01 g and these are weighed collectively and their average mass is then recorded. Fragment thickness is measured on those pieces that exhibit both inner and outer surfaces in order to determine strain-at-failure. Once material failure occurs, fragment deformation terminates and the measured thickness is presumed to coincide with that of failure [9]. Representative AerMet® 100 alloy fragments are shown in Figure 7.

5. Results

Soft capture analysis

For the AerMet® 100 alloy test discussed here, we recovered about 67% of the total metal cylinder mass. Fragments representing 59% of the recovered mass were suitable for making thickness measurements. The remainder did not exhibit both an inner and outer surfaces that were well defined, or the fragments were so narrow that we could not get a reliable thickness measurement. For the AerMet® 100 alloy rings, we recovered 75% of the original ring mass and made measurements on 722 fragments whose total weight was 210 grams, or 88% of the recovered mass.

* Based on Bernoulli's equation and using the UTS of the virgin steel.

Figure 8 shows the fracture strain distribution for the AerMet® 100 cylinder fragments both as through-thickness strain (bottom scale) and *net* eps (top scale). The through-thickness strain is defined as:

$$\varepsilon_{tt} = -\ln\left(\frac{t_{final}}{t_{initial}}\right) \tag{2}$$

where t_{final} and $t_{initial}$ are the final and initial thicknesses of the material. The mean and median ε_{tt} at fracture is 0.19 with a standard deviation of 0.032. Assuming cylinder expansion is plane strain, an equivalent plastic strain (eps) at fracture can be defined as:

$$\bar{\varepsilon} = \frac{2}{\sqrt{3}}\varepsilon_{tt} \tag{3}$$

where $\bar{\varepsilon}$ is the plane strain eps. $\bar{\varepsilon}$ is a *net* eps based on thickness. The fracture strain data for both the cylinder and ring configurations are summarized in Table 2.

Final thickness and final height of the ring segments were measured and the eps at fracture for the rings is determined from:

$$\bar{\varepsilon} = \frac{2}{\sqrt{3}}\left[\varepsilon_h^2 + \varepsilon_t^2 + \varepsilon_h \cdot \varepsilon_t\right]^{1/2}, \tag{4}$$

where ε_h and ε_t are the measured logarithmic height and thickness strains, respectively. (Note that when $\varepsilon_h = \varepsilon_t$, $\bar{\varepsilon} = 2\varepsilon_t$). The data are summarized in the histogram in Figure 9. The mean eps at failure is 0.33 (median eps at fracture is 0.31) and the standard deviation is 0.086. These numbers can be compared with the mean (median) eps at fracture for the cylinder of 0.23 (0.22). The mean fracture strain for unixial stress is about 40% higher than for the plane-strain condition. Similar analyses were made for the AISI 1018 steel cylinder and rings. The data is also tabulated in Table 2 for this material.

Superimposed on the fracture strain histograms for the AerMet® 100 alloy and AISI 1018 steel cylinders and rings are Weibull probability distribution functions (pdf) that have been normalized to fit the total fragment count. A standard three-parameter Weibull pdf, which is frequently used in failure analysis [21], is expressed as:

$$f_{\varepsilon-fail} = \left(\frac{\beta}{\eta}\right)\left(\frac{\varepsilon-\varepsilon_0}{\eta}\right)^{\beta-1}\exp\left[-\left(\frac{\varepsilon-\varepsilon_0}{\eta}\right)^{\beta}\right] \tag{5}$$

where ε is taken as eps at fracture, and β and η are the shape and scale parameters, respectively. The third parameter, a location parameter, is needed to define a critical strain below which there is a zero probability the material will fail. This location parameter is defined as ε_0. The Weibull parameters for the curves shown are listed in Table 3. All the fracture strain distribution data are fitted with a β=2 distribution.

High-speed diagnostics

Figure 10 shows an optical image taken at 25 μs after the detonator is fired; the detonator and booster pellet are located at the top of the picture. This type of optical image provides a snapshot of the entire deformation history of the cylinder spanning unperturbed, undeformed material (bottom) to completely fractured and fragmenting (top). Careful examination of these images reveals changes in texture that can be associated with the failure of the material. Using this image, the instantaneous cylinder diameter at three locations along the cylinder axis is calculated to determine the net diametric (circumferential) strain as a function of axial position. The three locations on the image are near the minimum fracture strain as defined by the Weibull pdf (ε_{tt}=0.15), the peak of the Weibull distribution (ε_{tt}=0.20), and the tail of the Weibull pdf (ε_{tt}=0.31). It is apparent that only for the higher strains is there any visible damage to the outside surface of the cylinder. And even for ε_{tt} =0.31, there is no apparent indication of smoke leaking through the cracks. The x-ray image of the cylinder taken at approximately the same time shows qualitatively similar features to those in the optical image.

The velocimetry monitored the outer surface of the cylinder at four different locations along its length: z = 3.81 cm, 7.62 cm, 11.43 cm and 14.24 cm (z=0 is the detonator end of the *cylinder*). The results of the measurement at one location for an AerMet® 100 alloy cylinder are shown in Figure 11 along with the results of two different CALE simulations. In the simulation with strength on, the agreement with the experiment is quite good for the first four or five microseconds when the cylinder starts to move. Later in time though, the measurement shows a higher velocity than the calculated one. With strength in the metal turned off in the simulation (treated as purely hydrodynamic), we see that there is better agreement between measurement and simulation later in time (after four or five microseconds). In the actual experiment, the

cylinder fractures in the 4-5 μs interval following initial expansion and therefore as discussed below, this would appear as a lack of strength retarding the outward expansion of the cylinder.

Metallurgical and metallographic analysis of the recovered fragments

AerMet® 100 alloy

Sample fragments from an AerMet® 100 alloy cylinder are shown in Figure 7. The aspect ratio of the fragments (length to width) is on the order of four or five—the mean fragment length is on the order of 16 mm and fragment widths are typically a few mm. Shear fractures running parallel to the fragment length define the fragment width while blunt fractures define the fragment length. A cross-section view of the fragment, perpendicular to its length shows the fracture surfaces to be either parallel or near perpendicular to each other.

A closer inspection of the inner and outer surfaces of the fragments, as shown in Figure 7, reveals a hierarchy of surface cracks that are not present in the pretest material. These surface cracks are all oriented parallel to the cylinder axis, and range from small micro-cracks to complete fracture. The length of the micro-cracks is typically on the order of a mm and have separations on the order of 200 microns. These longitudinal surface cracks penetrate on the order of tens of microns into the material. On a larger scale, a few dominant longitudinal cracks that are associated with shear bands penetrate more deeply into the material. These shear bands, associated with these cracks, are separated on a mm length scale. These shear bands are oriented at a plus/minus 40- to 45-degree angle to the surface (see Figure 19), and appear to result in shear fractures that can change orientation along the fracture surface; that is, it can switch from +45º to -45º on the same surface.

Figure 12 shows a cross-section of a fragment. Within the fragment interior, numerous adiabatic shear bands formed during cylinder deformation but do not result in fracture surfaces. Typically, these ASB have a spatial frequency of about 1/mm. Figure 12b shows a detail of the shear bands at the surface of the fragment in Figure 12a. These shear bands manifest themselves as steps on the surface of the fragment and account for the cracking seen in Figure 7. It is interesting to note that many of these fractures do not propagate all the way through the material; rather they only go to one surface. These ASBs can intersect other cracks propagating orthogonal to them. Thus it appears that these crisscrossing shear bands may inhibit their

overall mobility. The width of the ASB in the heat-treated material is about 1 μm, and nanoindentation hardness measurements of the material in the shear band indicate that the material is about 17% harder than the surrounding matrix material.

The dynamically deformed microstructure of soft AISI 1018 steel fragment differs significantly than that of hard AerMet® 100 alloy. In the AerMet fragments, strain localization induced deformation produces predominantly ASB, but in the AISI 1018 steel there is no visible ASB formation. Figure 13a displays a cross-sectional view of a fragment. Deformation twinning of the ferrite grains (Figure 13b) and cracks from coalesced MnS inclusions are apparent (Figure 13c). Dark regions in Figure 13b are the pearlite. However, the MnS inclusions control the fracture behavior of the steel by providing crack initiation sites and propagation paths into the material. Deformation twinning of ferrite grains is distinctly evident.

6. Discussion

Thickness measurements of recovered cylinder fragments (or transverse measurements of recovered ring fragments) are used to determine the stain at fracture for these geometries. At the onset of material fracture, a stress relief wave rapidly propagates through the fragment inhibiting further thinning of the material. The material comprising the fragment is assumed to have deformed uniformly prior to fracture and that significant levels of internal cavitation do not exist in the fragment interior.

Although ε_{tt} is calculated based on the fragment thickness, this strain does not reflect the deformation that the material experiences during the passage of the HE shock wave. As such eps is employed to characterize the strain accumulated during the initial shock loading and subsequent cylinder expansion. Figure 4 illustrates the relationship between eps and ε_{tt} as a function of time for the AerMet® 100 alloy. We use these curves to convert the measured ε_{tt} at fracture to the true eps at fracture. Thus, the mean ε_{tt} at fracture for the AerMet® 100 alloy cylinder of 0.20 corresponds to a mean eps (true) of 0.36. We apply the same correction to the eps (net) for the rings. Similar simulations and corrections are made for the AISI 1018 steel.

The Johnson-Cook fracture model represents the eps-triaxiality conditions at fracture. This model is a five-parameter empirical model that describes the fracture strain as a function of stress triaxiality, strain rate and homologous temperature. It is expressed analytically as:

$$\varepsilon^f = \left[D_1 + D_2 \exp D_3 \frac{\sigma_m}{\bar{\sigma}} \right] \times \left[1 + D_4 \ln \frac{\dot{\varepsilon}}{s^{-1}} \right] \times \left[1 + D_5 T^* \right], \qquad (6)$$

where the three brackets correspond to the stress triaxiality term, the strain rate term, and the homologous temperature. The first part that describes the stress triaxiality is a generalization of the Hancock-McKenzie model [22] that assumes D_3 is equal to 1.5, based on a theoretical model of spherical void growth [23]. Since we conducted all the experiments at the same strain rate and the same ambient temperature, we ignore these terms. Furthermore, since for each material we tested two different triaxial stresses and determined a mean strain at fracture for each, we have two equations and three unknowns (D_1, D_2 and D_3). We make the assumption that D_3=3/2 as in the original Hancock-McKenzie model. Table 4 lists the values of D_1 and D_2 for AerMet® 100 alloy and AISI 1018 steel determined from both the true eps at fracture (based on thickness strain corrected for initial shock deformation of the material) and the net eps at fracture (based on thickness measurements and, in the case of the cylinder, corrected for the plane-strain stress state).

Interpreting radiographs and optical images to determine failure and fracture is both difficult and misleading. Fine scale cracks exhibit very little contrast in the x-ray image or are not resolvable in the high-speed film images. Shadowing due to the double-pass radiographic technique can confound crack identification by overlapping cracks on opposing sides of the cylinder. Cracks that are oriented at an oblique angle with respect to the x-ray source also produce very little contrast on the x-ray image. Therefore for practical considerations, readily discernable cracks, *i.e.*, well-developed cracks that have opened sufficiently and provide adequate contrast on the radiograph, are those that are typically correlated with fracture. Optical imaging shows surface damage followed by HE reaction products (smoke) streaming through the fractured material. Correlating these cracks or the observation of smoke to circumferential strain and, if the load path is plane strain, to ε_{tt} suggests failure strains that exceed those based on direct measurements of recovered fragments. A simple computer code calculation suggests that there is a measurable time interval, on the order of a couple of microseconds, between material failure and the appearance of smoke. Considering

circumferential strain-rates on the order of ~0.05/μs, a 2μs time interval is equivalent to an additional strain of 0.10. Therefore failure strains based on crack (smoke) observation can be significantly larger than actual values.

In recovered AerMet® 100 alloy, evidence of non-uniform deformation in the form of shear bands and a minor degree of cracking and/or cavitation is observed. In the AISI 1018 steel we see twinning in the recovered fragments. Cracks are observed having penetrated into the material, thus creating open volume, but the extent is not believed to affect the ε_{tt} determinations. Evidence of isolated regions of non-uniform, deformation is observed. These localized regions consist of bands of highly deformed material oriented at approximately 45 degrees with respect to the cylinder wall surface. Nano-indentation measurements indicate that the shear band is harder than the shocked region; no further analysis was performed to characterize these shear bands. Also the role of the shear bands in the dynamic fracture process is not understood well.

Conclusion

We have measured fracture strain distributions for two different materials (AerMet® 100 alloy and AISI 1018 steel) under two different load paths (plane strain and uniaxial stress) driven by a high explosive. This unique drive imparts a plastic strain in the material that is not apparent in the final thickness of the material. Detailed numerical simulations are used to relate the final thickness of the fragments to the total eps up to the point where it fractures. Because the plane strain and uniaxial stress experiments were executed at the same strain rate, we can determine the parameters in the Hancock McKenzie model for fracture. This model is a constrained version of the more general Johnson-Cook fracture model.

For both materials we find that the uniaxial stress state has a significantly higher fracture strain than the plane strain case. We also find that the softer material, AISI 1018 steel, has a higher fracture strain than the harder AerMet® 100 alloy. This is consistent with the model originally proposed by G. I. Taylor.

Comparing the fracture strain data with the high speed imaging data, we find that the thickness measurements yield a lower fracture strain than would be inferred from either optical or x-ray images. Using smoke as the indicator of fracture significantly overestimates the fracture strain. Cylinder surface velocities determined with 2-D simulations of the explosively driven cylinder are in excellent agreement with

measurements up to the point of fracture when material strength is taken into account. The agreement after fracture is best when strength is turned off.

The two materials used in these studies are significantly different in their morphologies and their material properties. The AerMet® 100 alloy has a harder martensitic microstructure while the AISI 1018 steel comprises softer dual phases of ferrite grains and pearlite colonies. The materials fail in different ways as well. The AerMet® 100 alloy shows very little bulk damage to the martensite while numerous adiabatic shear bands populate the material with a subset of them participating in the creation of fracture surfaces. These ASB are very narrow (~ 1 μm) and are harder than the surrounding bulk material. The AISI 1018 steel on the other hand, exhibits deformation twinning of the ferrite grains in the bulk material and fracture results from coalesced MnS inclusions. Unlike the AerMet® 100 alloy, the AISI 1018 steel exhibits no ASB.

Acknowledgements

Authors would like to thank Stephen Holmes for engineering support in the design and fabrication of the experiments, Stephen Bosson for coordinating the assembly and execution of the experiments and the Bunker 851 staff for helping field the experiments. We would also like to acknowledge Paul Amala for help with the CALE simulations and Susan Mangels for help preparing this manuscript. This work was performed under the auspices of the U.S. Department of Energy by the University of California, Lawrence Livermore National Laboratory under Contract W-7405-ENG-48.

REFERENCES

1. Gurney RW. The Initial Velocity of Fragments from Bombs, Shells and Grenades. Army Ballistic Research Laboratory Report No. 405 1943

2. Taylor GI. Analysis of the Explosion of a Long Cylindrical Bomb Detonated at One End. Scientific Papers of G. I. Taylor, Vol. III No. 30. Cambridge University Press, 1963, p 277-286

3. Mott NF. Fragmentation of Shell Cases. Proc Royal Soc. London A 1947; 189: 300-308

4. Taylor GI. The Fragmentation of Tubular Bombs. Scientific Papers of G. I. Taylor, Vol. III No 44. Cambridge University Press, 1963, p 387-390

5. Hoggatt RH, Recht RF. Fracture Behavior of Tubular Bombs. J Appl Phys 1968; 39 (3): p 1856-1862

6. Banks EE. The Ductility of Metals under Explosive Loading Conditions. J. Inst. of Metals 1968; 96: p375-378

7. Perrone N. On the Use of the Ring Test for Determining Rate-sensitive Material Constants. Experimental Mechanics 1968; p. 232-236

8. Mock W Jr., Holt WH. Fragmentation behavior of Armco iron and HF-1 steel explosive filled cylinders. J. Appl Phys. 1983; 54: p 2344-2351

9. Grady DE, Hightower MM. Natural Fragmentation o f Exploding Cylinders. In: Meyers MA, Murr LE, Staudhammer KP, editors. Shock Wave and High-Strain Rate Phenomena in Materials. New York: Marcel Dekker, Inc., 1992. p 713-720

10. Martineau RL.A Viscoplastic Model of Expanding Cylindrical Shells Subjected to Internal Explosive Detonations Los Alamos National Laboratory Report LA-13424-T 1998

11. Winter RE. Measurement of fracture strain at high strain rates. Proc. of the Second Conference on the Mechanical Properties of Materials at High Rates of Strain. Oxford England, 1979: p 81-89

12. Vogler TJ, Thornhill TF, Reinhart WD, Chhabildas LC, Grady DE, Wilson LT, Hurricane OA, Sunwoo A. Fragmentation of Materials in Expanding Tube Experiments. Int J Impact Engng. 2003; 29: p 735-746

13. Grady DE, Benson DA. Fragmentation of metal rings by electromagnetic loading. Exp Mech. 1983; 23:393-400

14. Carpenter Specialty Alloys, "Alloy Data: AerMet® 100 Alloy," 1995

15. Lloyd RM. Conventional Warhead Systems Physics and Engineering Design V. 179 American Institute of Aeronautics and Astronautics 1998

16. Tarver CM. Ignition and Growth Modeling of LX-17 Hockey Puck Experiments. Propellants, Explosives and Pyrotechnics 2005; 30 (2): 109-117

17. R. Tipton (private communication); see also Numerical Modeling in Applied Physics and Astrophysics, edited by R.L. Bowers and J.R. Wilson, Jones and Barlett, Boston, 1991.

18. Steinberg DJ, Cochran SG, Guinan MW. A constitutive model for metals applicable at high-strain rate. J Appl Phys 1980;51 (3): 1498-1504

19. Johnson GR, Cook WH. Fracture Characteristics of Three Metals Subjected to Various Strains, Strain Rates, Temperatures and Pressures. Eng Fract Mech 1985; 21 (1): p31-48

20. AyerR, Machmeier P. On the characteristics of M_2C carbides in the peak hardening regime of AerMet 100 steel Metall. Mater. Trans. A. 1998; 29A:903-905

21. Hahn GJ, Shapiro SS Statistical Models in Engineering 1967 John Wiley & Sons, New York

22. Hancock JW, McKenzie AC. On the Mechanisms of Ductile Failure in High-strength Steels Subjected to Multi-axial Stress-states. J. Mech. Phys Solids 1976; 24: p 147-169

23. Rice JR, Tracey DM. On the Ductile Enlargement of Voids in Triaxial Stress Fields. J Mech Phys Solids 1969; 17: p201-217

Table 1. Selected AerMet® 100 alloy and AISI 1018 steel properties

	AerMet® 100 alloy (heat treated)	AISI 1018 steel (as-received)
Density	7.96 g/cm^3	7.87 g/cm^3
Sound speed (longitudinal)	0.578 cm/μs	0.37 cm/μs
Hardness	55 (Rockwell C)	135 (Vickers)
Elastic modulus	197 GPa	195 GPa
Yield strength	1.824 GPa	0.240 GPa
UTS	1.991 GPa	0.436 GPa
Fracture strain (quasi-static tensile test)	0.14	0.26

Table 2. Fracture strain for AerMet® 100 alloy and AISI 1018 steel cylinder and rings

	AerMet® 100 alloy cylinder	AerMet® 100 alloy rings	AISI 1018 steel cylinder	AISI 1018 steel rings
ε_{tt} (mean)	0.19	---	0.40	---
ε_{tt} (median)	0.19	---	0.40	---
standard deviation (ε_{tt})	0.032	---	0.06	---
net eps (mean)	0.22	0.33	0.46	0.56
net eps (median)	0.22	0.31	0.46	0.55
standard deviation (eps)	0.033	0.09	0.07	0.11

Table 3. Weibull parameters for fracture strain for AerMet® 100 alloy and AISI 1018 steel cylinders and rings

	β	η	ε_o
AerMet® 100 alloy cylinder	2.0	0.06	0.14
AerMet® 100 alloy rings	2.0	0.17	0.17
AISI 1018 steel cylinder	2.0	0.103	0.3
AISI 1018 steel rings	2.0	0.21	0.375

Table 4. Hancock-McKenzie (constrained Johnson Cook) parameters for AerMet® 100 and AISI 1018 steel based on net eps at fracture and true eps (corrected for initial shock deformation)

	D_1		D_2	
	true eps	net eps	true eps	net eps
AerMet® 100 alloy	0.00	0.00	0.86	0.54
AISI 1018 steel	0.24	0.24	1.11	0.54

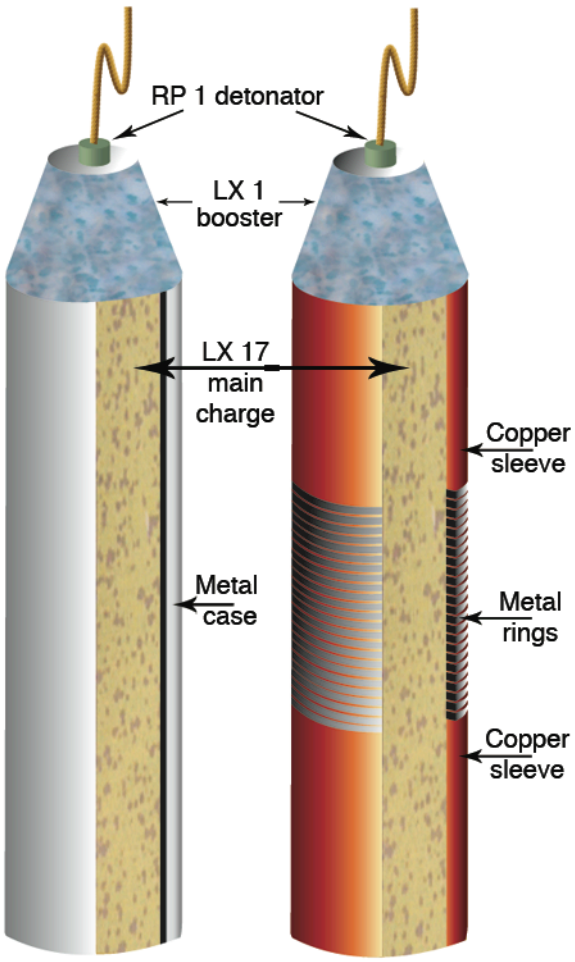

Figure 1 Schematic of standard cylinder to investigate plane strain and ring loaded cylinder to investigate uniaxial stress.

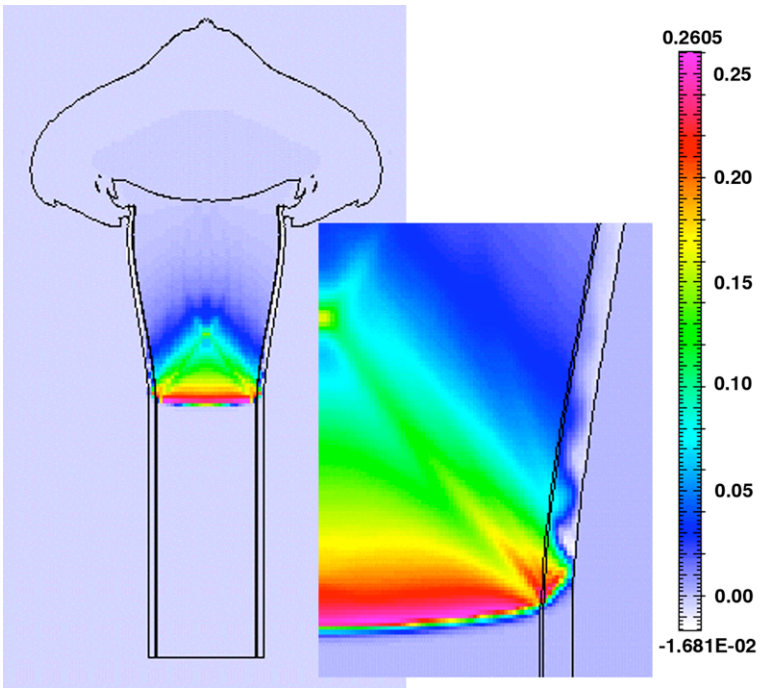

Figure 2 CALE simulation results of pressure in cylinder at 15 ms after detonation. Details show shock obliquity in wall. Contours are in Megabar

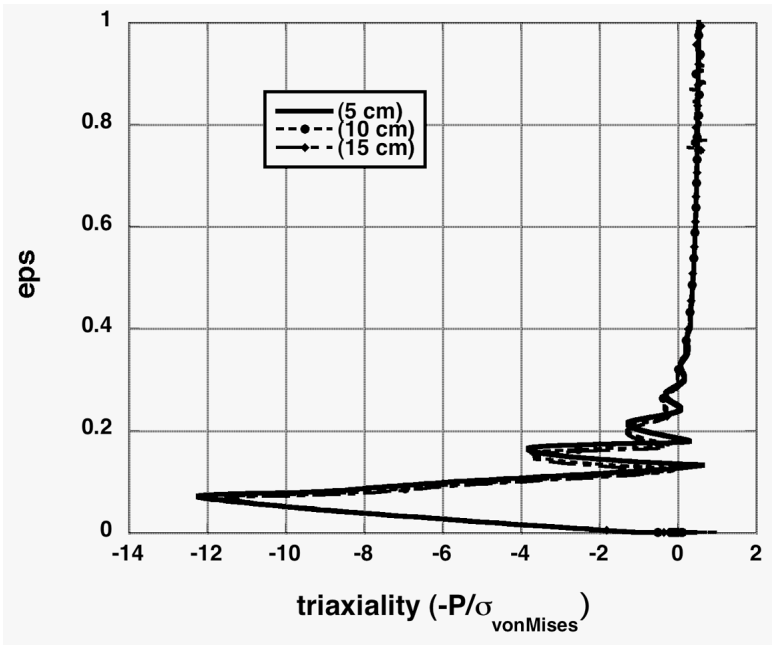

Figure 3 Calculated equivalent plastic strain as a function of triaxial stress at three locations in the pipe illustrating the uniformity of load path along the cylinder.

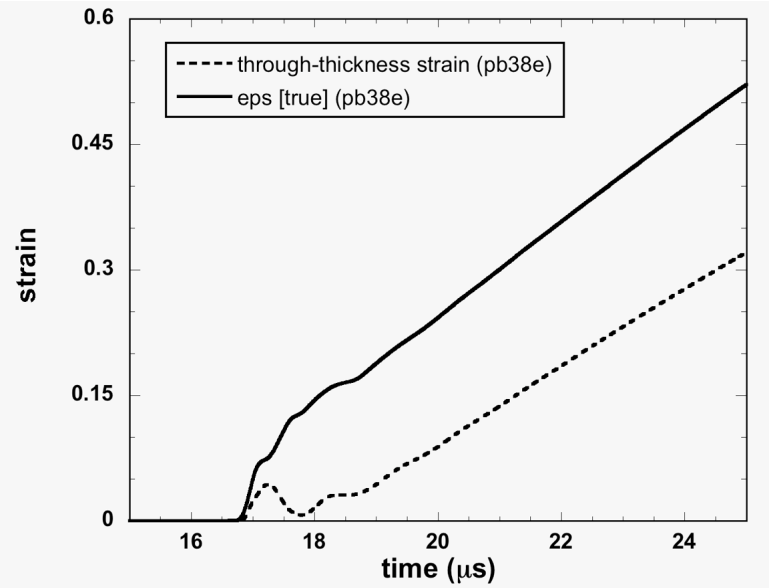

Figure 4 Calculated eps and through thickness strain as a function of time at one location in the cylinder. The difference between these strains corresponds to the shock induced strain as the detonation wave passes.

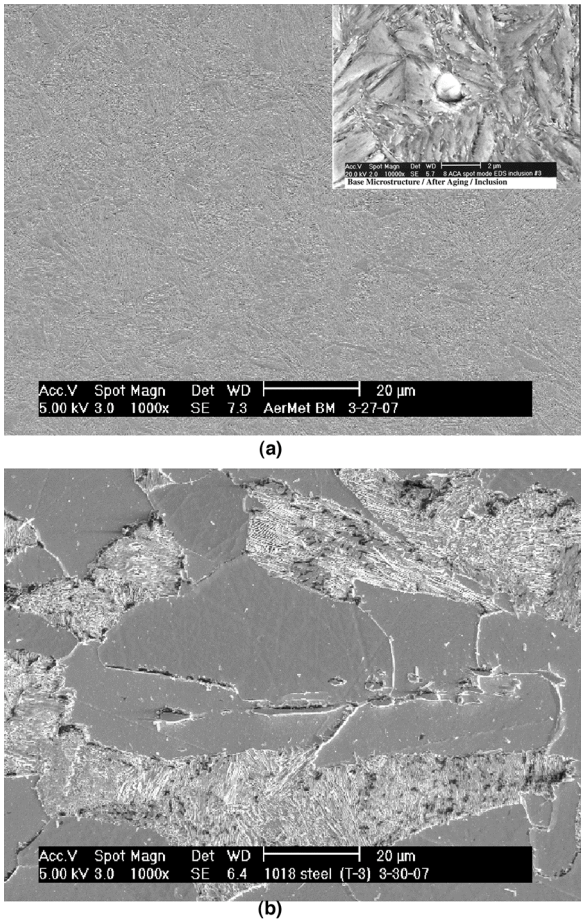

Figure 5. Microstructure of AerMet® 100 alloy and AISI 1018 steel

Figure 6 Schematic of soft capture tank that allows free expansion of the cylinder in air before initial retardation in the foam.

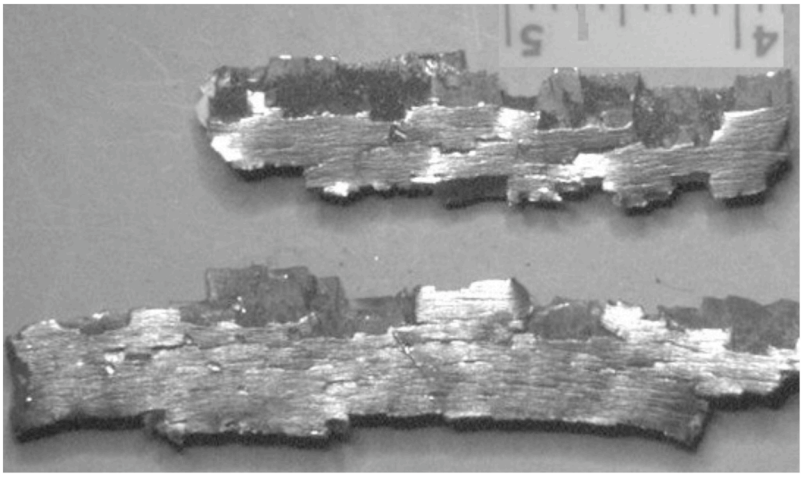

Figure 7 Recovered AerMet® 100 alloy fragments Note the roughened surfaces which correspond to a hierarchy of cracks that propagate varying distances into the material and the pronounced shear defining the fracture surfaces

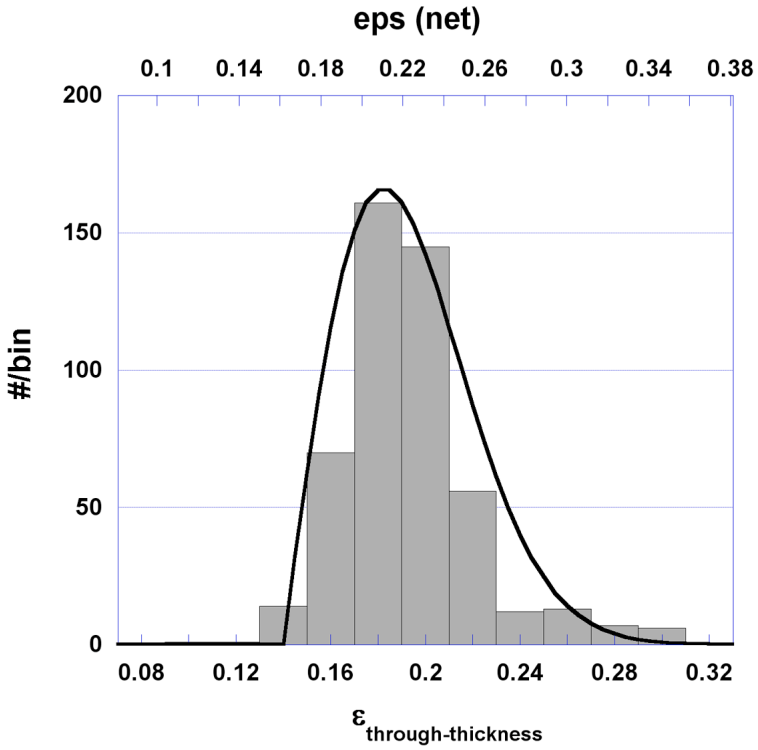

Figure 8 Histogram of fracture strain for fragments from AerMet 100 cylinder. Bottom scale corresponds to through thickness strain ($\varepsilon_{\tau t}$) and top scale corresponds to net eps ($=2\varepsilon_{tt}/\sqrt{3}$). Curve corresponds to Weibull distribution.

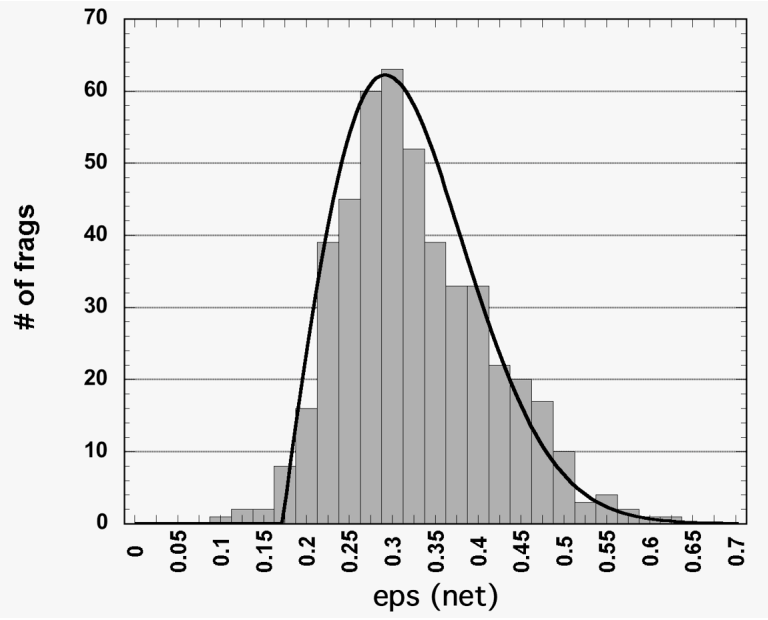

Figure 9 Histogram of fracture strain for fragments from AerMet 100 rings. $\varepsilon_{\tau t}$ is defined in equation 4. Curve corresponds to Weibull distribution.

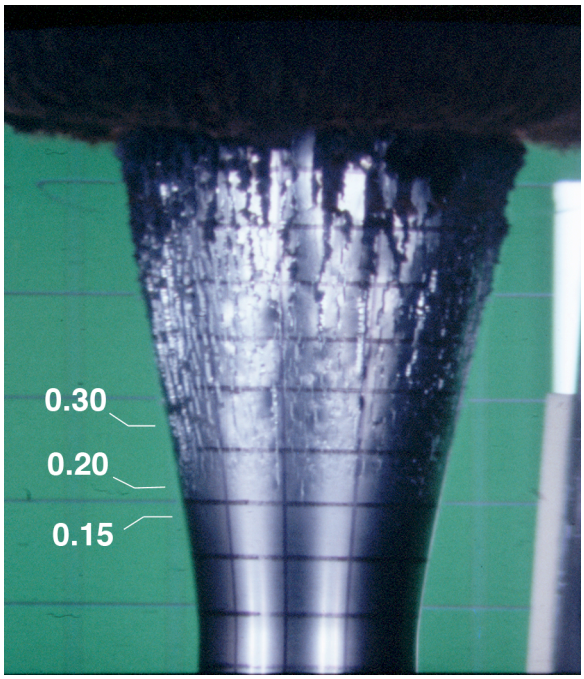

Figure 10. Optical image of exploding AerMet® 100 alloy cylinder 25 ms after detonation. Markers indicate circumferential strain that can be directly compared to corresponding through thickness strain

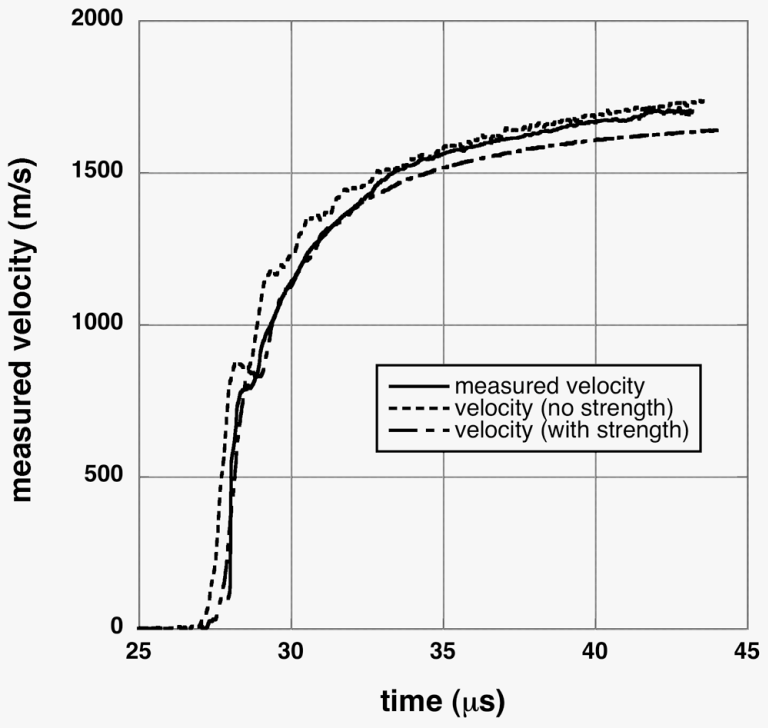

Figure 11. Measured and calculated cylinder expansion velocity. Simulations correspond to metal cylinder with and without strength.

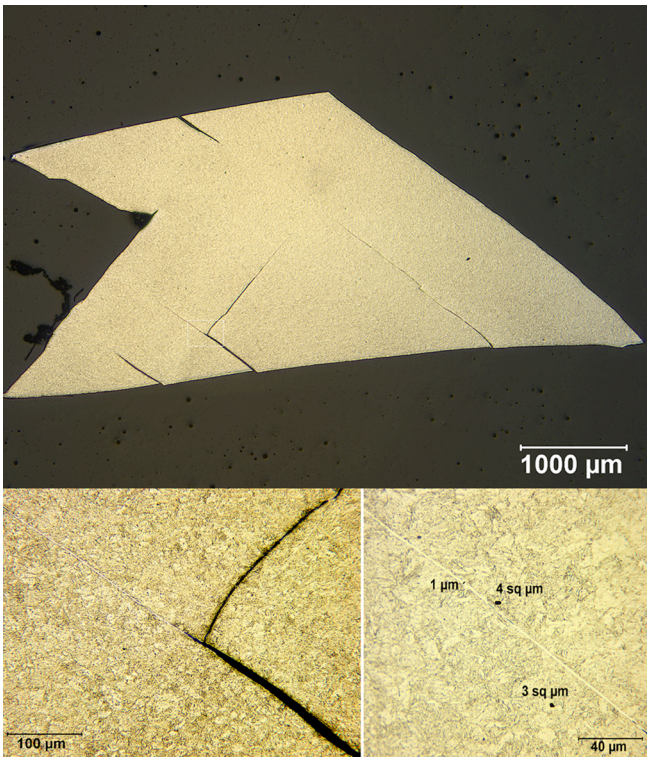

Figure 12. Cross section of AerMet 100 alloy fragment showing shear band population through fragment (a), intersecting shear bands (b) and shear band morphology (c)

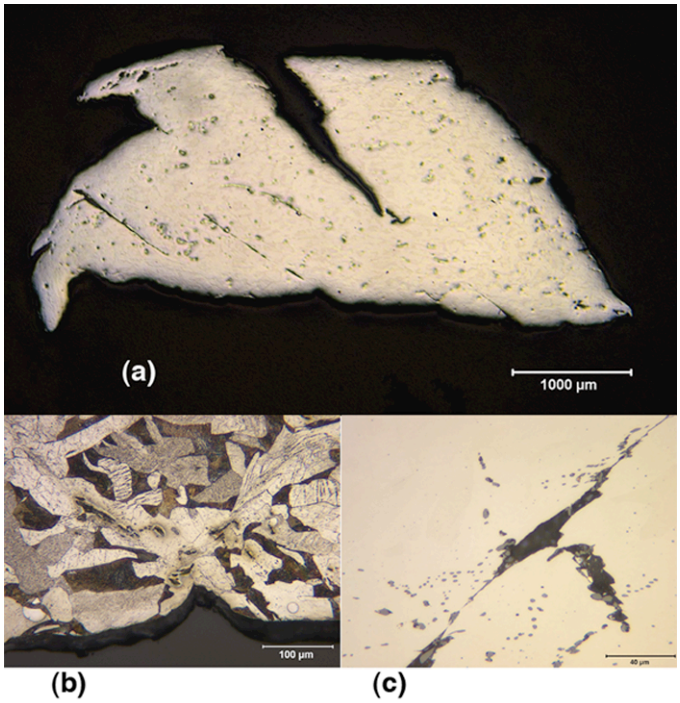

Figure 13 Cross section of AISI 1018 steel fragment showing bulk deformation through fragment (a), twinning in the ferrite; dark regions are pearlite (b) and coalesced MnS inclusions (c)